RSC Advances

PAPER

View Article Online
View Journal | View Issue

Cite this: *RSC Adv.*, 2026, **16**, 7178

A bidirectionally conductive composite membrane based on copper-coated electrospun PI-CNT fibers as a current collector for lithium-ion batteries

Jianghui Liu,[a] Shuya Liu,[b] Lili Zhao,[a] Yujun Luo,[a] Yini Ran,[a] Mohan Tang,[a] Guilin Shi,[a] Yuxin Liu,[a] Jianglan Lin,[a] Maoxian Wang,[a] Zhengnan Li,[a] Zhen Yao,[a] Zhusheng Yang [a] and Hai Fu *[a]

This study aims to reduce dependence on copper while enhancing the energy density of lithium-ion batteries. Plastic-based current collectors (PBCCs) offer a promising approach to replace copper, minimize the proportion of inactive material, and ultimately increase the energy density of lithium-ion batteries. A key challenge involved the synergistic optimization of the PBCC's conductive framework and its interfacial surface properties. Herein, a PI-CNT-Cu composite membrane was constructed by depositing copper onto electrospun PI fibers containing CNTs. This hierarchical architecture coupled the intrinsic longitudinal conductivity of the CNT network within the fibers with the transverse conductivity of the continuous copper layer, resulting in a composite membrane with a volumetric conductivity of 5.6 $\times$ 10^3 S cm^{-1}. In the electrochemical performance evaluations, graphite anodes employing PI-CNT-Cu CCs exhibited a capacity retention of 95.29% after 190 cycles at 0.5C. The performance enhancement could be attributed to the markedly rougher surface of the PI-CNT-Cu CC (Sa = 2.668 μm) relative to copper foil (Sa = 0.938 μm). This morphology enhanced the contact area and adhesion with the electrode layer, which was crucial for maintaining the structural integrity of the electrode during long-term cycling. In contrast to copper foil, the PI-CNT-Cu CC, with its fiber-woven structure, exhibited a significantly lower areal density with identical thickness values. The capacity of the anode electrode, was calculated based on the total mass including active materials and CCs. Utilizing PI-17%CNT-Cu exhibited significantly higher discharge capacities of 81.7 mA h g^{-1} at the same rates compared to the Cu foil at 35.08 mA h g^{-1}.

Received 29th December 2025
Accepted 29th January 2026

DOI: 10.1039/d5ra10075e

rsc.li/rsc-advances

1 Introduction

With the continuous expansion of the markets for electrical energy storage and power transmission, the demand for copper increased. However, the price of copper was subject to cost volatility and long-term escalation, primarily due to the fragile supply chain, including mining instability and capacity limitations in the smelting industry. As a result, the strategy of "replacing copper with polymers" emerged as a promising research trend. This approach aimed to substitute key components like copper foil current collectors (CCs) in lithium-ion batteries, thereby diversifying the range of available materials. Furthermore, lithium-ion batteries with high gravimetric energy density were capable of storing more electrical energy at the same mass, making the development of batteries with enhanced energy density a central challenge in battery research.[1–3] Researchers significantly improved the energy density of lithium-ion batteries through modification strategies such as elemental doping, surface coating, and interface engineering of active materials.[4–6] Alternatively, reducing the proportion of inactive components in batteries presented another promising approach to enhancing the gravimetric energy density of lithium-ion batteries.

Although CCs served as secondary components in lithium-ion batteries, they played a critical role in collecting and distributing electrical current.[7,8] Copper had been the conventional material of choice for CCs in batteries, serving as the essential pathway for the reversible conversion between chemical and electrical energy due to its superior conductivity and stability.[9] Compared to copper, plastic materials possessed a lower density, which directly reduced the mass of inactive components. However, the development of plastic-based current collectors (PBCCs) had a series of strict requirements: ensuring sufficient electrical conductivity to enable efficient electron transport; exhibiting robust chemical and electrochemical stability to withstand complex internal battery environments; maintaining adequate

[a]*School of Materials and Architectural Engineering (Guizhou School of Emergency Management), Guizhou Normal University, Guizhou 550025, China. E-mail: fullsea@yeah.net*

[b]*School of Chemical Engineering and Technology, Tianjin University, Tianjin 300350, China*

mechanical robustness to guarantee structural integrity; and achieving strong adhesion with coated electrode materials.[10,11]

Topical research on PBCCs paid considerable attention to process feasibility, which led to the design of a sandwich-structured battery CC consisting of "metal layer-polymer layer-metal layer". This architecture significantly enhanced the energy density of lithium-ion batteries through lightweight design, while utilizing the inherent electrical insulation and thermal stability of the polymer to improve battery safety.[12] Fu *et al.*[7] successfully fabricated a lightweight, highly conductive PI@Cu composite CC *via* electroless copper plating, which achieved uniform copper deposition. This collector not only reduced battery weight but also improved both energy density and rate capability. When paired with a lithium titanate anode, the cell maintained a capacity retention rate exceeding 95% after 100 cycles at 0.5C. Sun *et al.*[13] fabricated a high-performance PBCC using a polyimide-based polyurea substrate coated with copper on both sides *via* magnetron sputtering. The N–H and C=O groups in the polyimide-based polyurea facilitate strong interfacial adhesion through electron donation from lone pairs on nitrogen atoms to the vacant orbitals of copper, resulting in a current collector with high interfacial strength, excellent flexibility, and enhanced safety. The corresponding cell achieved a significant improvement in energy density, corresponding to a 61% enhancement. This work served as an exemplary demonstration of molecular interfacial engineering for high-performance PBCC. Nevertheless, for the electrospun fibers PBCCs, including those based on PI, PP, and PET, inadequate mechanical strength and poor interfacial stability remained persistent and ubiquitous challenges in reported studies.[14–16] Therefore, further systematic research on structural design and interfacial optimization of PBCC was necessary.

This work presented a novel lightweight PI-fiber membrane fabricated *via* an electrospinning process and electroless copper plating. The material combines low areal density with mechanical flexibility, achieving a coordinated design that integrates structural and functional advantages. The electrospun fibers formed a continuous three-dimensional conductive network, effectively shortening electron transport pathways and enhancing conductive efficiency. Importantly, the microscale undulating structure of the fibrous mat was preserved after copper coating, resulting in a roughened PI-CNT-Cu interface. This roughness interface not only increased the contact area with the electrode slurry but also established multiple physical anchoring sites, which synergistically enhanced interfacial charge transfer and mechanical adhesion. Benefiting from these structural merits, cells employing the PI-CNT-Cu CC demonstrated superior electrochemical performance. In summary, the lightweight, bidirectionally conductive PI-CNT-Cu CC developed herein offered a promising and practical solution for advancing high-energy-density lithium-ion batteries.

2 Experimental section

2.1 Materials

Carbon nanotubes (CNTs, diameter: 10–20 nm, length: 1–2 μm), *N*,*N*-dimethylacetamide (DMAc), 3,3′,4,4′-biphenyltetracarboxylic dianhydride (BPDA), and 4,4′-oxydianiline (ODA) were purchased from Aladdin. Copper sulfate pentahydrate ($CuSO_4 \cdot 5H_2O$), potassium sodium tartrate ($NaKC_4H_4O_6$), ethylenediaminetetraacetic acid disodium salt (EDTA-2Na), sodium hydroxide (NaOH), potassium ferrocyanide ($K_4Fe(CN)_6$], 2,2-bipyridyl ($C_{10}H_8N_2$), formaldehyde (HCHO) solution (40 wt%), and silver nitrate ($AgNO_3$) were obtained from Sigma-Aldrich. The anode active materials, graphite (P15-X) powders, were purchased from Shanshan Reagent Co., Ltd. Carbon black (Super P) and polyvinylidene fluoride (PVDF) were acquired from Timcal and Suwei Co., Ltd., respectively. Ultra-pure water with a resistance higher than 18 MΩ cm was used to prepare solutions and wash samples.

2.2 Preparation of the PI-CNT membranes

Firstly, 1.07 g CNTs were dispersed in 20 mL DMAc and ultrasonicated for 1 hour to produce a uniform suspension. Subsequently, under ice bath (0–5 °C), equimolar amounts of BPDA and ODA monomers were added successively. The reaction system was stirred under a nitrogen atmosphere for more than 16 hours to obtain a PAA-17%CNT composite solution. The nanofiber membrane was prepared using an electrospinning device under the following parameters: a collection distance of 20 cm, a solution feeding rate of 1 mL h^{-1}, a voltage of 16 kV, and a spinning duration of 4 hours. The ambient temperature was maintained at 25 ± 2 °C, with relative humidity kept at a controlled level of 40 ± 5%. The as-obtained PAA-CNT nanofiber membranes were imidized in a tubular furnace under programmed heating to obtain PI-CNT. The heating process involved the following four steps: (1) raising temperature from room temperature to 100 °C at 3 °C min^{-1} and holding for 1 hour; (2) increasing temperature from 100 to 200 °C at 3 °C min^{-1} and holding for 1 hour; (3) ramping up temperature from 200 to 350 °C at 3 °C min^{-1} and holding for 2 hours. Finally, the PI-17%CNT was obtained when the membrane cooled down. Specifically, the PI-10% CNT and PI-15% CNT membranes were prepared using the same process.

2.3 Preparation of PI-CNT-Cu

The prepared PI-CNT membranes were immersed in a 15 wt% NaOH solution for 60 minutes to activate the membrane surface. Following this, the PI-CNT membranes were immersed in a 1 g L^{-1} $AgNO_3$ solution for 10 minutes to facilitate the adsorption of silver ions onto the membrane surface, thereby enhancing the catalytic activity for subsequent copper deposition. Finally, PI-CNT membranes were immersed in an electroless copper deposition (ECD) bath. The ECD bath was prepared by dissolving 15 g of $CuSO_4$, 14 g of potassium sodium tartrate, 20 g of EDTA-2Na, 15 g of NaOH, 10 mg of $K_4[Fe(CN)_6]$, 20 mg of 2,2′-bipyridyl, and 15 mL of formaldehyde in 1 L of deionized water under constant stirring. Samples with CNT additions of 10%, 15%, and 17% were designated as PI-10%CNT, PI-15%CNT, and PI-17% CNT, respectively. The activated PI-10% CNT, PI-15% CNT, and PI-17% CNT membranes were treated for durations of 45, 90, 135, and 180 minutes, respectively. After each treatment, the membranes were rinsed three times with deionized water.

Subsequently, the rinsed membranes were dried at 60 °C for 12 hours, yielding the final PBCCs designated as PI-10%CNT-Cu, PI-15%CNT-Cu, and PI-17%CNT-Cu.

2.4 Preparation of the anode electrodes

Graphite was selected as the anode active material (nominal capacity: 372 mA h g^{-1}). To prepare the coating slurries, graphite, PVDF, and Super-P were mixed with a weight ratio of 8 : 1 : 1 in NMP solvent. Cu, PI-10%CNT-Cu, PI-15%CNT-Cu, and PI-17%CNT-Cu CCs were directly coated with graphite slurry for anode electrode fabrication. The coated samples were then transferred to a vacuum drying oven and dried at 105 °C for 12 hours to remove residual solvent. The resulting active material layer had an approximate thickness of 40 μm. The dried electrodes were subsequently calendared using a roll press with a gap set to 10 μm.

The calendared electrodes were then punched into 14 mm diameter disks using a precision die. The punched electrodes were returned to the vacuum drying oven and dried at 55 °C for 5 hours to ensure any remaining moisture was eliminated. Finally, the mass of each electrode disk was accurately measured and recorded. The loading of active materials was 1.17 mg cm^{-2} for graphite electrodes for a half-cell assembly.

2.5 Cell assembly and testing

The coin cells were assembled in a glove box under an argon atmosphere with moisture and oxygen levels maintained below 0.01 ppm. In the cell configuration, the electrodes with different CCs were used as the working electrode, and a lithium metal was utilized as the counter electrode. The cell was assembled in a bottom-to-top configuration: negative shell, lithium metal foil, separator, electrolyte, working electrode, spacer, spring sheet, and top case (positive shell). The electrolyte was 1 M lithium hexafluorophosphate ($LiPF_6$) in ethylene carbonate (EC)/diethyl carbonate (DEC) = 1 : 1 (v/v). A volume of 40 μL of the liquid electrolyte was added to each cell, and Celgard 2500 was used as the separator. The rate performance and cycling stability of the half cells were evaluated using the Neware battery testing instrument within a voltage window of 0.005–2 V. The cyclic voltammetry (CV) and electrochemical impedance spectroscopy (EIS) performance were tested on a CHI 760E electrochemical workstation, with the voltage range set from 0.005 to 2 V and the frequency sweep from 100 kHz to 10 MHz.

2.6 Characterization

The surface and cross-sectional morphologies of samples were characterized by a ZEISS Sigma 300 scanning electron microscope (Germany) with a voltage of 16 kV. The elemental composition and crystal structure were analyzed using a Thermo Scientific K-Alpha X-ray photoelectron spectrometer (XPS, USA) and X-ray diffraction (XRD, 40 kV and 40 mA, $\lambda = 0.15406$ nm, scan range: 5–80°, scan step: 10° min^{-1}). Thermal stability and weight loss behavior were evaluated by thermogravimetric analysis (TGA, STA 449 F3 Jupiter) from 40 °C to 800 °C with a heating rate of 10 °C min^{-1}. Fourier transform infrared (FTIR) spectroscopy (BRUKER Tensor 27) was employed to determine the molecular functional groups. The electrical conductivity of the PI, PI-10%CNT, PI-15%CNT, and PI-17%CNT samples was measured using a four-point probe resistivity measurement system. The contact angles were measured under standardized conditions: deionized water for the PI-CNT membranes and *N*-methyl-2-pyrrolidone (NMP) for the PI-CNT-Cu membranes.

3 Results and discussion

3.1 Preparation and characterization

Due to its exceptional electrochemical stability, polyimide (PI) was selected as the supporting layer for plastic-based current collectors (MPCCs). The introduction of conductive fillers can significantly enhance the electrical conductivity of polymer PI, but excessive addition not only compromises the mechanical properties of the composite materials but also poses challenges to processing techniques and cost control. To address this, the research team precisely incorporated carbon nanotubes (CNTs) into the polymer PI matrix by adjusting their addition ratio. By combining electrospinning technology and electroless copper plating processes, a PI-CNT-Cu composite membrane with bidirectional conductivity was successfully fabricated. Fig. 1a illustrates the preparation process of PI-CNT-Cu MPCCs.

As shown in Fig. 1b, the apparent color of the composite membranes was observed to change visibly. The PI-CNT membrane exhibited carbon-black coloration. After ECD treatment, however, the membrane surface presented the characteristic metallic orange-red color of copper metal. This pronounced color transition conclusively indicated the formation of a continuous metallic copper layer on the PI-CNT membrane. Additionally, the image provided clear visual evidence of the significant flexibility and bendability of the PI-based composite membranes.

Fourier-transform infrared (FTIR) spectroscopy was employed to analyze the evolution of functional groups before and after imidization. As shown in the FTIR spectrum of PAA-CNT (Fig. 1c), the characteristic absorption peaks at 1715 cm^{-1}, 1653 cm^{-1}, 1548 cm^{-1}, 1495 cm^{-1}, and 1376 cm^{-1} can be assigned to the asymmetric stretching vibration of C=O in COOH, symmetric stretching vibration of C=O in CONH, asymmetric stretching vibration of CO–NH, skeletal vibration of the benzene ring, and symmetric stretching vibration of CO–NH, respectively. These absorption features were consistent with the functional groups presented in the molecular structure of PAA. After thermal imidization, the FTIR spectrum of PI-CNT composite membrane exhibited characteristic absorption bands at 1772 cm^{-1}, 1720 cm^{-1}, 1493 cm^{-1}, 1363 cm^{-1}, 1237 cm^{-1}, and 724 cm^{-1}, which correspond to the asymmetric stretching of C=O, symmetric stretching of C=O, skeletal vibration of the benzene ring, C–N stretching vibration, ether bond vibration, and C=O bending vibration, respectively.[17–19] The disappearance of the absorption peaks at 1653 cm^{-1} and 1548 cm^{-1}, along with the emergence of peaks at 1363 cm^{-1} and 1237 cm^{-1}, clearly demonstrated the successful conversion of PAA-CNT into PI-CNT.[20]

Thermal analysis of the PAA-CNT composite membranes in N_2 atmosphere was carried out, all samples exhibited two main

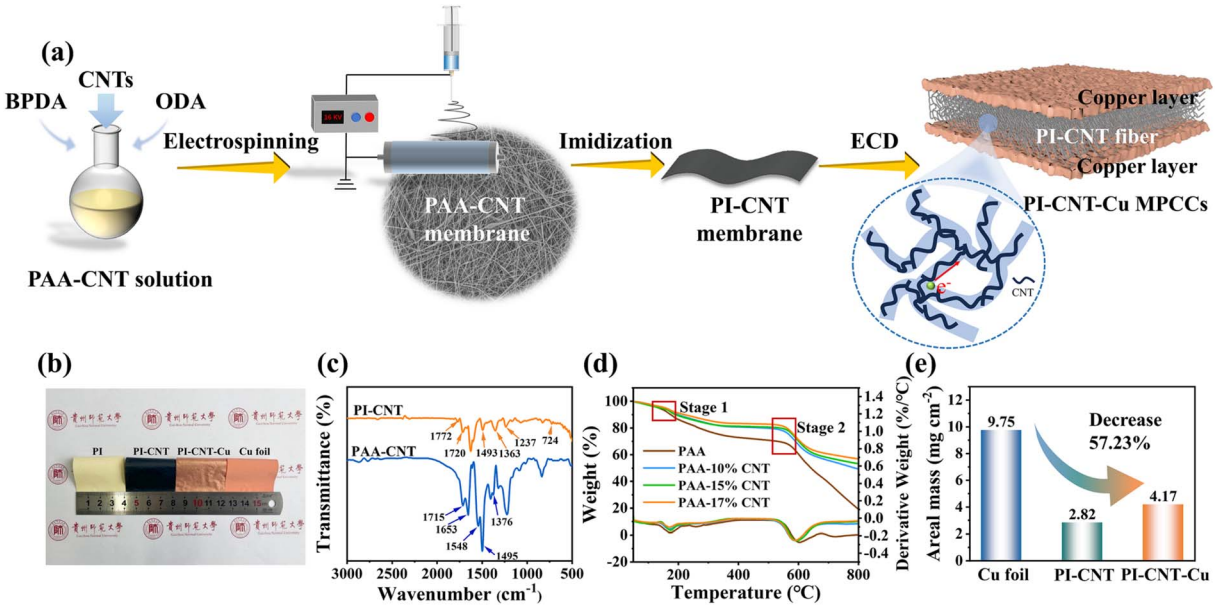

Fig. 1 (a) Preparation of the PI-CNT-Cu MPCCs. (b) Optical photographs of PI, PI-CNT, PI-CNT-Cu composite membranes, and Cu foil. (c) FTIR spectra of PAA-CNT and PI-CNT composite membranes. (d) TG analysis of PAA-CNT composite membranes with varying CNT contents. (e) Areal mass comparison among Cu foil, PI-CNT, and PI-CNT-Cu composite membrane.

stages of weight loss (Fig. 1d). The initial weight loss between 170 and 200 °C was attributed to the release of volatile components, including the desorption of physically adsorbed water and potentially water molecules released during the initial stage of thermal imidization of the PAA.[21–23] The subsequent temperature interval of 250–350 °C corresponded to the main weight-loss plateau associated with the imidization reaction of the PAA matrix. Finally, the pronounced weight-loss stage observed between 550 and 660 °C was attributed to the thermal decomposition of the PI backbone.[9] Based on the residual mass after heating, the actual CNT contents in the membranes were calculated, which aligned well with the nominal loadings. Furthermore, in terms of areal mass, the Cu foil has the highest value, with a density of 9.75 mg cm^{-2}, as shown in Fig. 1e. In contrast, the PI-CNT-Cu composite membrane exhibits a much lower areal mass of only ≈ 4.17 mg cm^{-2}, while exhibiting reductions of 57.23%.

The effect of CNT content on the morphology of the resulting electrospun PI-CNT fibers was systematically investigated. As depicted in Fig. 2a–d, the PI fibers displayed a uniform and smooth surface structure with an average diameter of approximately 2.32 μm, and no bead formation was observed.[24] With increasing CNT content from 10% to 15% and then to 17%, the average fiber diameters decreased markedly to 0.574 μm, 0.534 μm, and 0.442 μm, respectively. The phenomenon was primarily attributed to the increased solution concentration resulting from the addition of CNTs, which necessitated a higher applied voltage to enhance the electric field intensity during the electrospinning. The intensified electric field promoted splitting and stretching of the jet, thereby leading to the formation of finer fibers.[25–27] With further increase in CNT content (19%), severe bead formation occurred during the spinning process, leading to progressively deteriorated fiber uniformity and integrity, which had a detrimental effect on the overall architecture and uniformity of the electrospun membrane (Fig. S1).

XRD was conducted to investigate the crystallographic structure of PI-CNT composite membranes with varying CNT contents. As shown in Fig. 2e, the PI displayed a broad diffraction peak in the range of 12–30°, characteristic of its amorphous nature.[28] In contrast, the PI-CNT composite membranes exhibited a characteristic peak at $2\theta = 23°$, corresponding to the (002) graphitic plane of carbon nanotubes. With increasing CNT content, the intensity of this characteristic peak progressively increased, indicating a higher degree of graphitization within the composite structure. Considering both electrical conductivity and structural integrity, a CNT content of 17 wt% was selected for subsequent studies. With increasing CNT content, the electrical conductivity of the PI-CNT composite membranes exhibited typical percolation behavior.[29–31] Below the percolation threshold, charge transport relied on inefficient point-to-point tunneling, resulting in low conductivity. When the CNT content reached 17 wt%, the system surpassed the percolation threshold, forming a continuous three-dimensional conductive network, which significantly enhanced the conductivity to 0.1162 S cm^{-1} (Fig. 2f). Beyond this threshold, further addition of CNTs primarily contributed to densifying and optimizing the existing network, leading to a slowdown in the rate of conductivity enhancement and a trend toward saturation.

Consequently, the conductivity of the composite membrane was enhanced by nine orders of magnitude compared to that of the PI membrane.[32] The confinement effect of the one-dimensional PI fibers promoted the formation of interconnected CNT networks, which improved the overall electrical conductivity

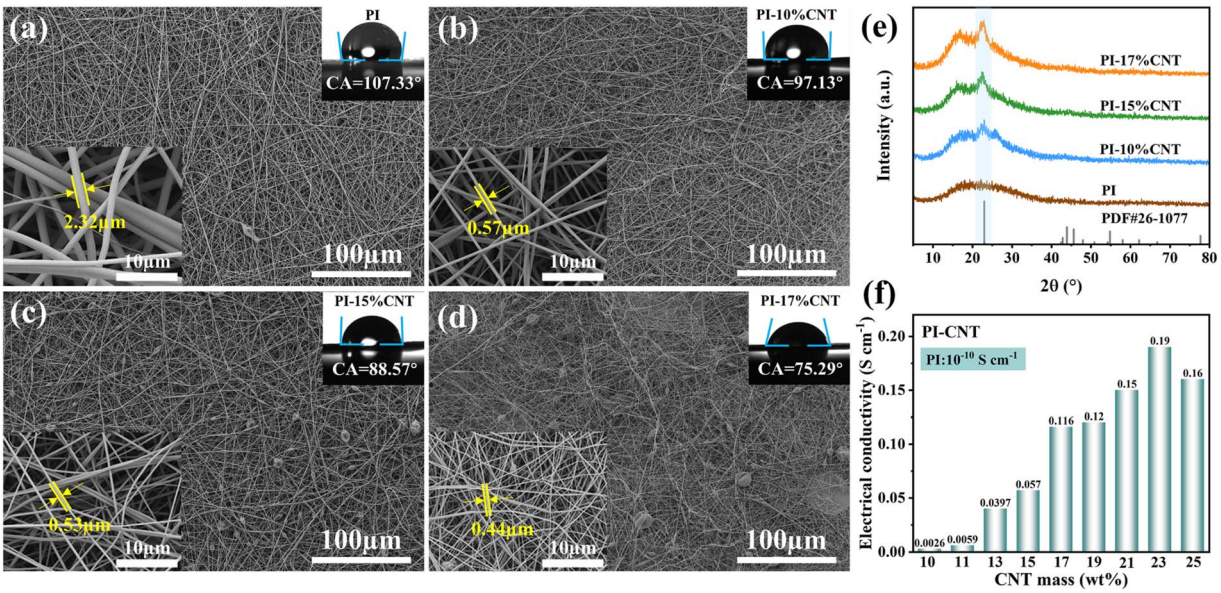

Fig. 2 SEM images of (a) PI, (b) PI-10%CNT, (c) PI-15%CNT, and (d) PI-17%CNT composite membranes; the insets show the surface contact angle of the membranes with deionized water. (e) XRD patterns of PI-CNT membranes at varying CNT contents. (f) Electrical conductivity of PI-CNT membranes at varying CNT contents.

of the fibrous membrane.[33] Additionally, the enhanced conductive contact sites formed on the surface of the fibrous architecture effectively optimized the adhesion interface between the subsequently deposited metal and the polymer layer.[34]

The inset in Fig. 2a–d shows the images of electrodes surface contact angle, with increasing CNT content, a marked decrease in the contact angle was observed for the PI-CNT composite membranes, signifying improved water wettability and, consequently, an enhanced hydrophilic character. The contact angle of the PI membrane was 107.33°, showing obvious hydrophobicity, which was determined by the non-polar chemical structure. The mass fraction of CNT increased gradually (10 wt%, 15 wt%, and 17 wt%), and the corresponding contact angles decreased to 97.13°, 88.57° and 75.29°, respectively. The phenomenon occurred because CNTs modified the composite surface characteristics. Specifically, the interfacial polarization between filler and matrix was intensified, leading to increased overall material polarity and thus higher surface energy.[35] From a morphological perspective, CNT incorporation compromised the smoothness and flatness of PI fiber surfaces, generating micro-scale uneven features. Consistent with the classical Wenzel wetting theory, this microscopic roughness amplified the material's inherent wetting characteristics,[36] endowing the enhanced PI-CNT composite membranes with hydrophilicity. The synergistic effect of enhanced polarity and surface roughness in PI-CNT composite membranes facilitated the transition of the fibrous membrane from a hydrophobic to a hydrophilic state. Video S1 demonstrated that following a 10 seconds immersion in aqueous solution, the pristine PI membrane floated on the liquid surface, whereas the PI-CNT composite membrane maintained its position at the bottom. The superior hydrophilicity exhibited by PI-CNT membranes enabled effective immersion in an aqueous copper sulfate solution.

3.2 Investigation of properties of PI-CNT-Cu membrane

The influence of electroless copper deposition (ECD) time on the surface characteristics of the PI-17%CNT membrane was revealed in the micrographs of Fig. S2. The deposition process triggered the imide rings in the molecular structure of PI to undergo ring-opening reactions, generating carboxyl (–COOH) and hydroxyl (–OH) groups, which significantly improved the hydrophilicity of the substrate surface.[24,37] The enhanced hydrophilicity directly contributed to stronger interfacial adhesion with the copper layer. The microstructure of the copper layer showed a clear trend of grain coarsening with prolonged ECD time. With the prolongation of ECD time, the particle size on the surface of the fiber membrane gradually increased, and the stacking was more compact. After 180 minutes of deposition, the electrical conductivity of the PI-17% CNT-Cu composite reached 5.6×10^3 S cm^{-1} (Fig. S3), exhibiting a four-order-of-magnitude improvement over the PI-17% CNT composite membrane. The XRD patterns (Fig. S4) displayed three distinct characteristic diffraction peaks at approximately 43.3°, 50.5°, and 74.1°, which can be indexed to the (111), (200), and (220) planes of face-centered cubic (fcc) copper, respectively. All diffraction peaks from the PI-based composite materials demonstrated excellent alignment with the standard copper pattern (PDF#04-0836), with these sharp and distinct peaks confirming high crystallinity of the deposited copper layer.

Given that surface characteristics like roughness and wettability were critical for the application performance of composite membranes, a comprehensive understanding of how the copper layer modulates these properties in the PI-CNT-Cu membrane was essential. Using the same ECD time, a copper layer was deposited on the surface of the PI-CNT membrane. Surface

roughness measurement (Fig. 3a–d) revealed that the PI-17% CNT-Cu membrane exhibited a significantly higher surface roughness (Sa = 2.668 μm) compared to the copper foil (Sa = 0.938 μm). The highly rough surface of PI-CNT membranes was effectively replicated onto the copper layer, resulting in PI-CNT-Cu membranes with a corresponding undulating morphology. Additionally, this markedly enhanced surface roughness was identified as the key factor responsible for the further reduction of contact angle.

As shown in the inset of Fig. 3a–d, the surface contact angle for the PI-17%CNT-Cu membrane was measured at just 8.62°, which was considerably lower than that of pure copper foil (22.94°), indicating its superior affinity for the NMP solvent. The extremely low contact angle (8.62°) of the PI-17%CNT-Cu membrane indicated its superior surface wettability, which facilitated the subsequent coating of active material slurry. This high wettability ensured rapid and uniform spreading and penetration of the electrode slurry onto the membrane surface. More importantly, the PI-CNT-Cu membrane with rough surface provided greater contact area and stronger physical adhesion.[38] At the current collector level, the surface roughness directly influenced the interfacial interlocking state between the collector and electrode materials, thereby affecting the electrode performance.[39,40] This reinforced interfacial bonding effectively suppressed the detachment of the active material layer caused by interfacial failure during long-term charge–discharge cycles. Through rationally modulating the surface of the PI substrate, the PI-based membranes were imparted with high roughness and improved wettability. Consequently, these surface properties of the PI-CNT-Cu membranes held the potential for excellent interfacial stability and superior electrochemical performance in lithium-ion batteries.

The conductive ability of the PI composite membranes was demonstrated through LED illumination devices, as shown in Fig. 4a and b. The deposited copper layers in both PI-17%CNT-Cu and PI-Cu exhibited a preference for transverse conductivity. This enabled independent current conduction through these metal layers, which successfully powered the LED illumination. However, in the PI-Cu configuration, the natural insulating properties of the polymer PI hindered longitudinal current transfer, rendering the LED nonfunctional (Fig. 4b). In marked contrast, the PI-17%CNT-Cu configuration achieved efficient longitudinal current conduction, successfully illuminating the LED due to the presence of the 3D conductive PI-17%CNT intermediate layer (Fig. 4a). These results provided strong evidence for the crucial role of the PI-17%CNT-Cu structure in

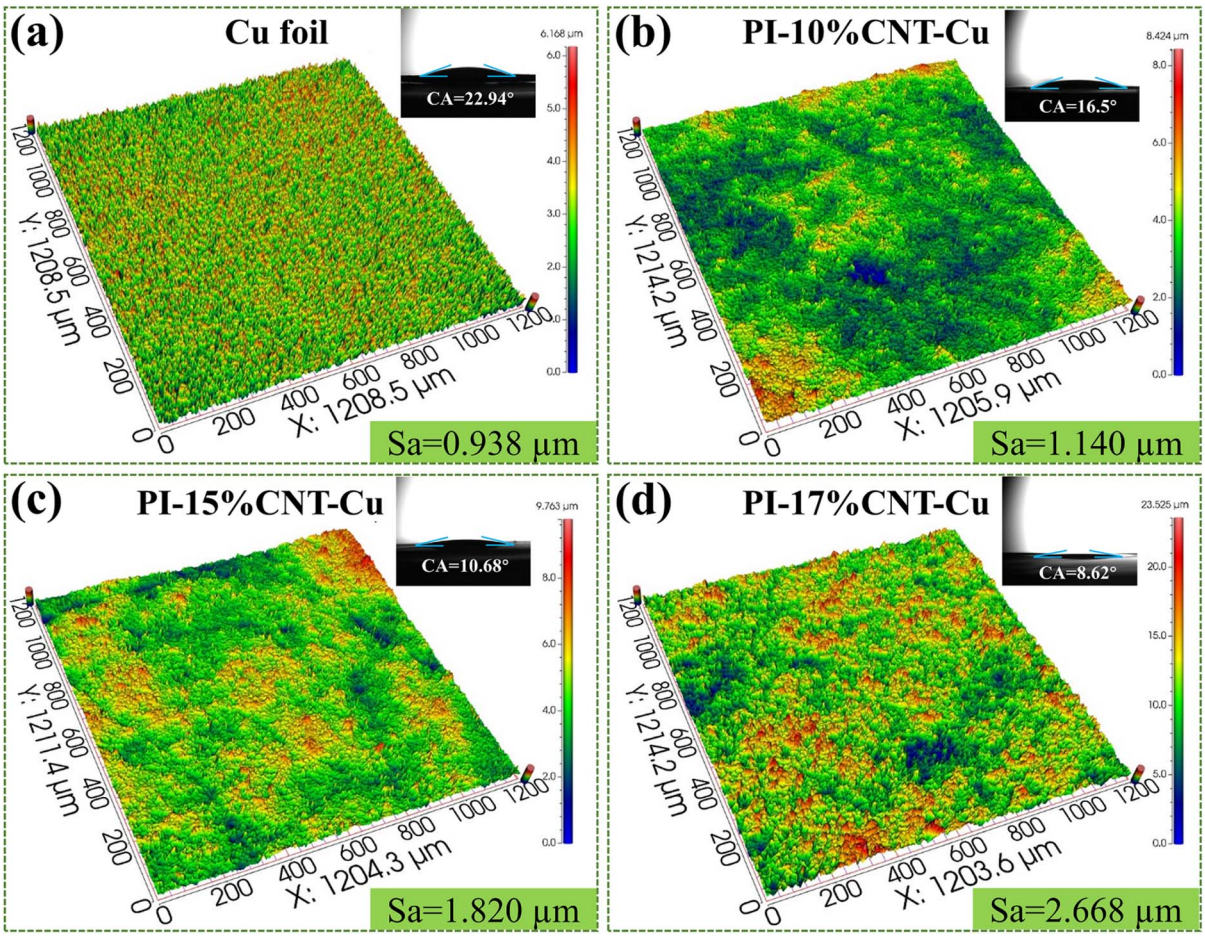

Fig. 3 Surface roughness of (a) Cu foil, (b) PI-10%CNT-Cu, (c) PI-15%CNT-Cu, and (d) PI-17%CNT-Cu composite membranes. The insets show the surface contact angle of the composite membranes with NMP.

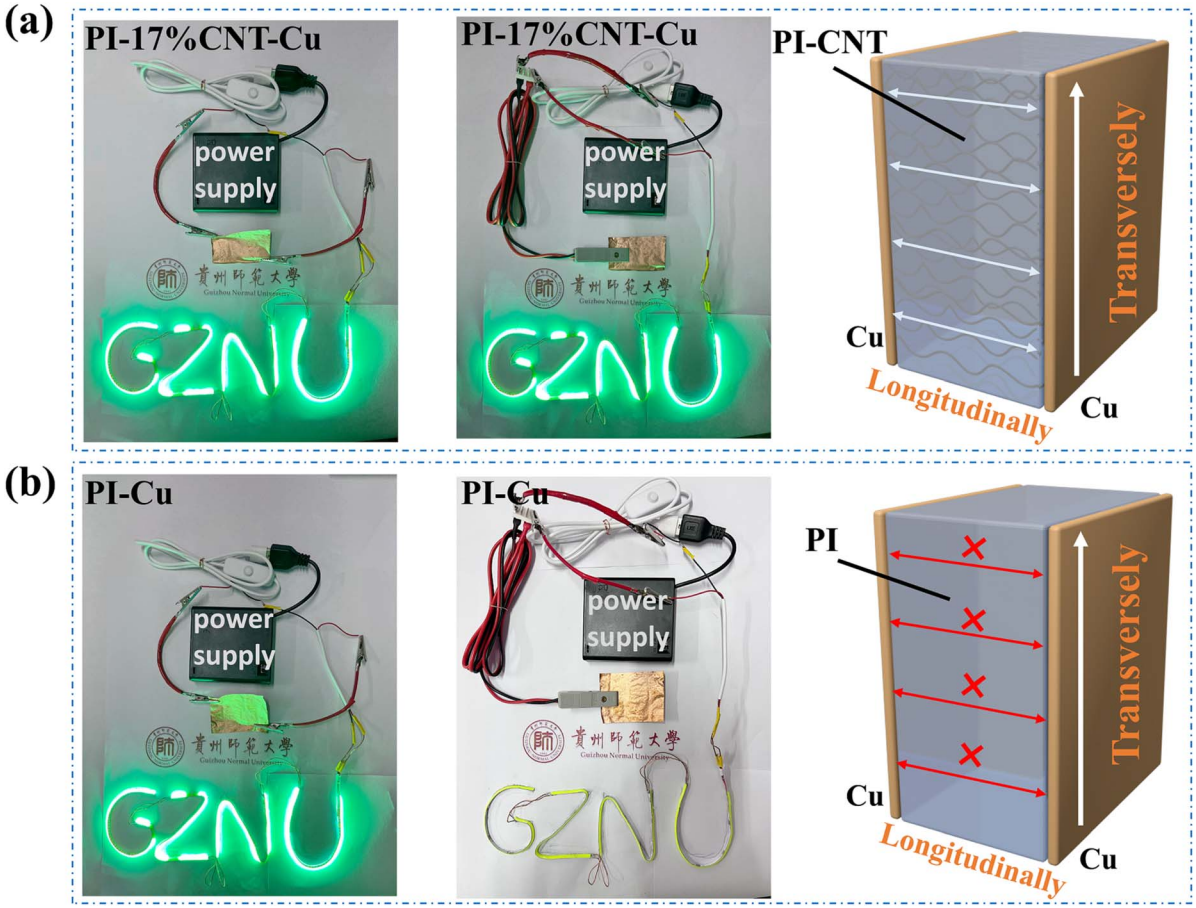

Fig. 4 A comparative visualization of the transverse and longitudinal electrical conductivity: (a) PI-17%CNT-Cu composite membrane, (b) PI-Cu composite membrane.

establishing conductive pathways along the longitudinal direction. Furthermore, temperature-dependent conductivity tests further highlighted the advantages of the PI-17%CNT-Cu membrane (as shown in Fig. S5). In a comparative analysis between copper foil and PI-17%CNT-Cu membrane, upon heating from 25 °C to 200 °C, the conductivity of the PI-17% CNT-Cu membrane decreased by only 36%, significantly lower than the 74.3% decrease observed for the Cu foil.

3.3 Electrochemical performance of half-cell

To investigate the influence of the CCs on the electrochemical performance of LIBs, half-cells were assembled and systematically evaluated. The CV curves of PI-17%CNT-Cu and Cu foil graphite electrodes were measured at a scan rate of 0.1 V s^{-1} between 0.005 and 2 V *vs.* Li^+/Li. As shown in Fig. 5a and b. The Cu foil electrode showed poor repeatability and significant fluctuations in its cyclic voltammetry curves, reflecting its limited cycling stability and reversibility. Conversely, the PI-17%CNT-Cu electrode exhibited highly reproducible curves, evidenced by the near-perfect overlap of its final two cycles. These observations confirm that the roughened surface of the PI-17%CNT-Cu current collector significantly improves the electrochemical reversibility of graphite electrodes. Outstanding rate performance suggests that the battery can effectively meet the conditions of high-power and high-rate discharge. As shown in Fig. 5c (the rate performance data were collected after cell activation), the PI-CNTs-Cu/graphite electrode delivered higher specific discharge capacities than the Cu/graphite electrode across all rates. At 2C, the discharge capacity of the Cu/graphite cell sharply decreased to 180.6 mA h g^{-1}, whereas the PI-17%CNTs-Cu/graphite cell maintained at 256.268 mA h g^{-1}. When the rate was restored to 0.1C, the capacity of the PI-17%CNTs-Cu/graphite cell recovered to its initial value.

To corroborate the above conclusions, morphological changes of the electrode surface before and after cycling were examined. As shown in Fig. 5d–f, both the PI-17%CNTs-Cu and Cu foil CCs exhibited comparable and homogeneous distributions of the anode slurry prior to cycling, with no apparent difference in coating quality. After cycling, however, pronounced detachment of electrode materials was observed on the Cu foil, exposing the bare Cu substrate (the circled area in Fig. 5g and g'). In contrast, the electrode layer on the PI-17% CNTs-Cu current collector remained intact and uniformly adhered, with no observable detachment (Fig. 5e and e'). These results indicated that the roughened copper surface of the PI-

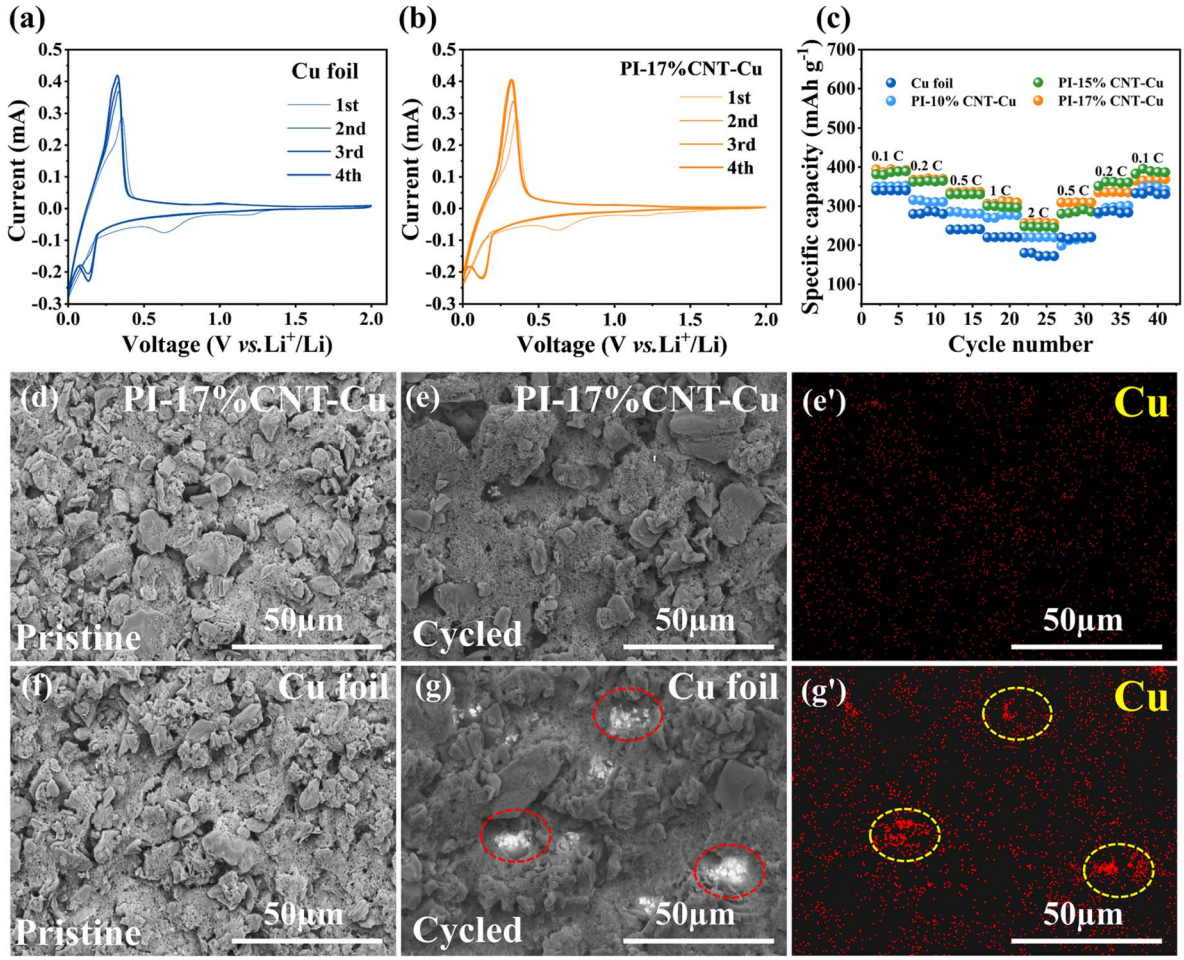

Fig. 5 CV performances of cells with (a) Cu foil and (b) PI-17% CNT-Cu CCs, (c) rate performance of cells with different CCs. SEM images of the electrode sheets (d) PI-17% CNT-Cu and (f) Cu foil before cycling, (e) and (g) present. SEM images of the cycled PI-17%CNT-Cu and copper foil electrodes, respectively, (e') and (g') show the corresponding surface EDS elemental mapping.

17%CNTs-Cu CC facilitated superior interfacial contact with the electrode material, even under high-rate conditions, thereby contributing to a higher discharge capacity.[41–45]

Fig. 6a demonstrated the initial charge–discharge profiles of commercial graphite in the voltage range of 0.005∼2 V at a current density of 0.1C (1C = 372 mA h g^{-1}). The cells based on PI-17%CNT-Cu exhibited discharge specific capacities of 404.41 mA h g^{-1}, which was higher than that of Cu foil (370.10 mA h g^{-1}). It can be explained that parts of CNTs were involved in the intercalation/deintercalation of Li ions. The corresponding coulombic efficiency was achieved of 80.44% and 78.32%. Thus, whether considering the initial discharge specific capacity or coulombic efficiency, PI-CNT-Cu/graphite electrodes exhibited higher values than Cu/graphite electrode. This was because increased actual contact area allowed a larger electron conduction channel, which improved electron conduction efficiency and the initial coulombic efficiency. During the initial charge/discharge cycles, a solid electrolyte interphase (SEI) film forms on the surfaces of graphite particles and the electrode, and its properties critically determine the overall performance of the electrode.

The long-term cycling performance of cells assembled with different CCs at 0.5C and 1C current densities was presented in Fig. 6b and c. The cell employing PI-17%CNT-Cu CC maintained a higher specific discharge capacity of 385.38 mA h g^{-1} compared to that of the Cu foil (327.86 mA h g^{-1}) after 190 cycles. At the same time, the cell of PI-17%CNT-Cu exhibited a superior capacity retention of 95.29%, outperforming the Cu foil, which retained only 88.37% of its initial capacity. To explore the cycling performance difference between the two CCs, the research compared the SEM images of the electrodes before cycling and after 300 cycles at 1C.

As shown in Fig. S6, the adhesion between the electrode slurry and the PI-17%CNT-Cu collector was superior to that with the copper foil before cycling. After cycling, however, a more pronounced interfacial gap was observed between the copper foil and the electrode layer (Fig. 6d). By contrast, the electrode layer on the PI-17%CNT-Cu CC remained intact and uniformly adherent without cracks (Fig. 6f). Demonstrating significantly stronger interfacial bonding. As illustrated in Fig. 6e, the relatively smooth surface of the Cu foil resulted in poor interfacial adhesion with the electrode layer. Due to the restricted contact

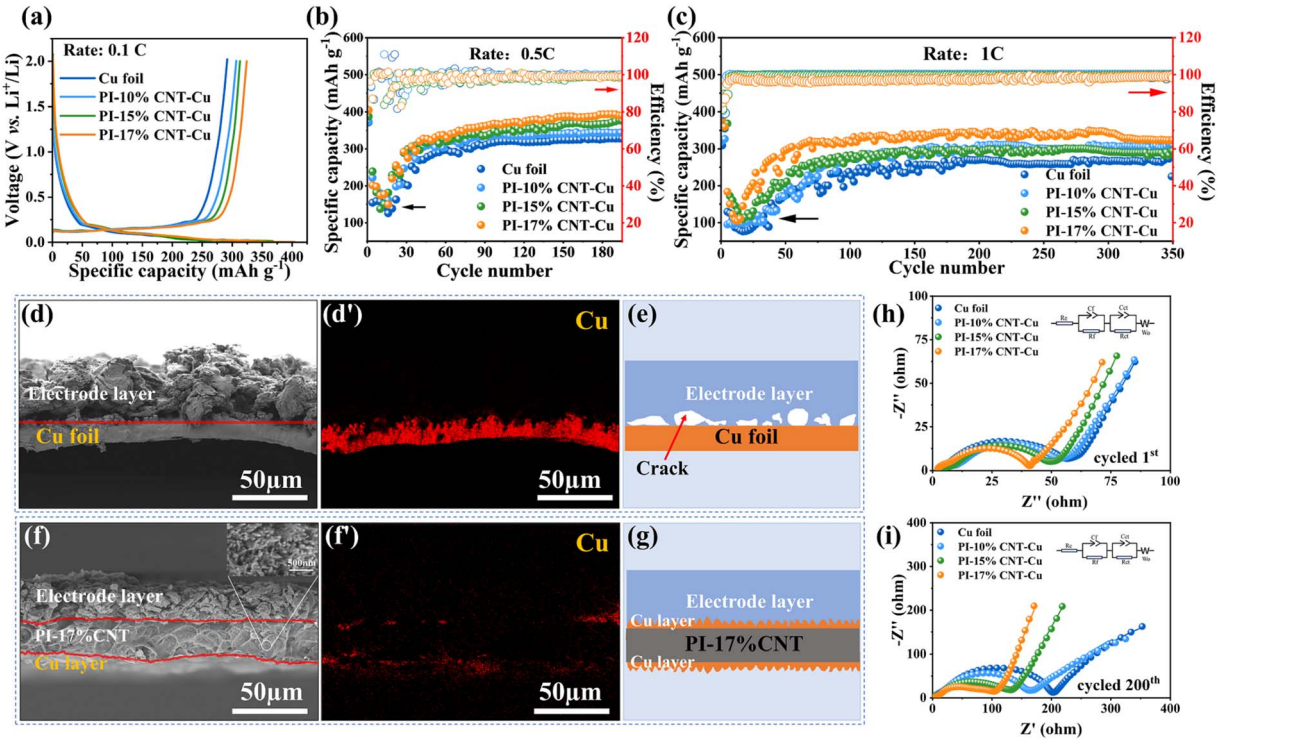

Fig. 6 (a) Initial cycle charge/discharge curves of cells with different CCs at 0.1C between 0.005 and 2.0 V. Long-term cycling stability of cells with different CCs at (b) 0.5C and (c) 1C. Cross-sectional SEM images of cycled electrodes on (d) Cu foil and (f) PI-17%CNT-Cu, accompanied by their corresponding Cu elemental mappings from EDS analysis (d') and (f'). Schematic illustrations of electron transfer at the interface between the electrode layer and the two types of CCs: (e) Cu foil and (g) PI-17%CNT-Cu. Nyquist plots of cells with different CCs after (h) 1 cycle and (i) 200 cycles. The inset is the equivalent circuit.

area at the electrode layer and copper foil interface, electron transfer was hindered, which gave rise to the observed low capacity. However, the rough surface of the Cu layer enhanced the contact area with the electrode layer and provided more electron transport channels to reduce the contact resistance (Fig. 6g).[46,47] This structural advantage contributed to the superior long-term cycling performance observed in cells employing the PI-17%CNT-Cu CC.

EIS of cells with different CCs was determined to investigate the interfacial stability. The EIS curves of the PI-CNT-Cu/graphite and the Cu/graphite electrode were plotted in Fig. 6h and i. The EIS curves consisted of semicircles in the high-frequency region and a sloping line in the low-frequency region.[48] The EIS curves were fitted using the equivalent circuit shown in the inset of Fig. 6h to extract the charge transfer resistance (R_{ct}) of cells employing different CCs. After the first cycle, the R_{ct} values for cells based on PI-17%CNT-Cu and Cu foil CC were 33.5 Ω and 55.04 Ω, respectively. After 200 cycles, these values increased to 76.2 Ω and 181.2 Ω (Fig. 6h, i and Table S1). Although the electrical conductivity of the PI-CNT-Cu CCs was inferior to that of the Cu foil CC, it still exhibited lower impedance values. This was primarily due to the rough surface of the PI-CNT-Cu CC, which provides a larger interfacial contact area and enhances interfacial adhesion, thereby significantly reducing the charge-transfer resistance at the interface.[49,50] More importantly, the internal CNT network enabled short-path electron transport and uniform current distribution, mitigating local overpotential and consequently lowering the overall activation energy required for charge transfer. These combined effects ultimately led to a lower R_{ct}.

Currently, the gravimetric capacity of the electrode was typically evaluated based solely on the mass of the active materials, without accounting for the contributions from inactive components such as current collectors, conductive agents, and polymeric binders. Herein, we compared the gravimetric capacity of PI-17%CNT-Cu/graphite and the Cu/graphite electrode based on the whole mass of the electrode. The areal mass of each component in the two electrodes was shown in Fig. 7a. The results indicated that in the Cu/graphite electrode, the graphite active material accounted for only 10.7% of the total mass. In contrast, benefiting from the lightweight characteristics of the PI-17%CNT-Cu CC, the mass ratio of graphite to the PI-17%CNT-Cu/graphite electrode increased to 21.20%. When calculated based solely on the mass of active materials, the gravimetric capacity of the graphite/PI-17%CNT-Cu electrode was 385.38 mA h g^{-1} at 0.5C, which was only 17.54% higher than that of the graphite/Cu electrode (327.86 mA h g^{-1}) (Fig. 7b). However, the gravimetric capacity of the graphite/PI-17%CNT-Cu electrode was 81.7 mA h g^{-1} at 0.5C based on the total electrode mass, representing an enhancement of more than 132.89% compared to the 35.08 mA h g^{-1} of the graphite/Cu electrode. Notably, the PI-CNT-Cu CCs developed have already demonstrated significant advantages even at a greater thickness than copper foil. Should the preparation process be

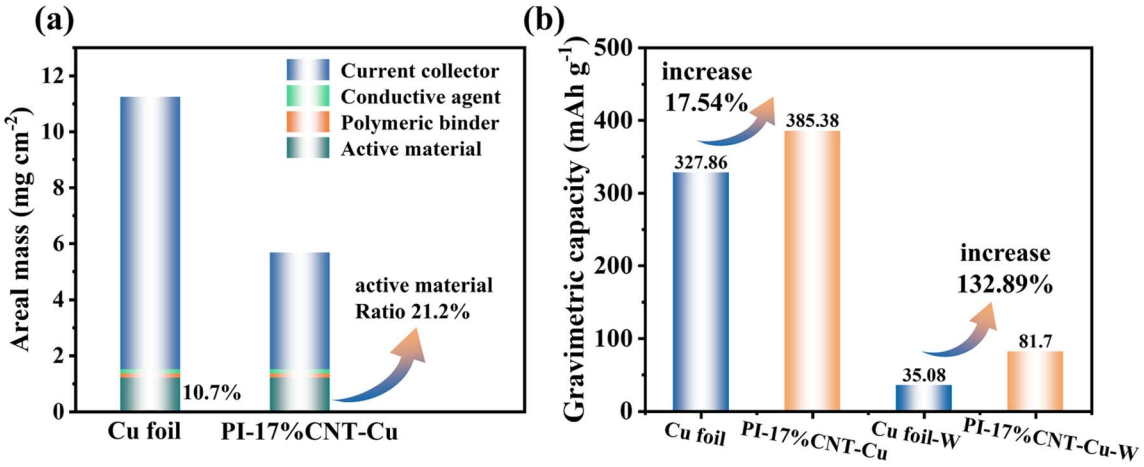

Fig. 7 (a) Comparison of areal masses of the Cu/graphite and PI-17%CNT-Cu/graphite electrodes; (b) comparison of the gravimetric capacity of Cu/graphite and PI-17%CNT-Cu/graphite electrodes based on the mass of active materials and the whole electrode (Cu foil-W and PI-17%CNT-Cu-W).

further optimized to yield thin PI-CNT-Cu composite membranes, it was anticipated that the overall gravimetric capacity of batteries could be substantially enhanced.

4 Conclusion

In summary, we successfully designed the PI-CNT-Cu composite membranes *via* electrospinning and electroless copper plating methods. This was accomplished through the substitution of the traditional copper foil CC with PI-CNT-Cu CC, leveraging its lower density and integrated conductivity. With CNT addition of 17 wt%, the resulting PI-CNT membrane had diameter of 0.44 μm and achieved an electrical conductivity of 0.116 S cm^{-1}, which was nine orders of magnitude higher than that of the pristine PI fiber membrane. The resulting PI-17%CNT-Cu CC achieves electrical conductivity of 5.6×10^3 S cm^{-1}, with surface roughness of 2.668 μm for the PI-17%CNT-Cu compared to 0.938 μm for Cu foil. The battery assembled with PI-17%CNT-Cu CC demonstrated superior performance, with the graphite/PI-17%CNT-Cu electrode achieving capacity retention of 95.29% after 190 cycles at 0.5C. This performance enhancement was attributed to the deliberately engineered rough surface of the PI-CNT-Cu CC, which ensures durable adhesion with the electrode slurry and effectively mitigates the detachment of active material during cycling. Furthermore, when calculated based on the total electrode mass, including both active materials and the CC, the graphite/PI-17% CNT-Cu anode delivered a specific capacity of 81.7 mA h g^{-1} at 0.5C, representing an increase of over 132.89% compared to the 35.08 mA h g^{-1} of the Cu/graphite anode. Our strategy for the conductivity design and surface modulation of PBCCs offered a novel pathway toward next-generation CCs, enabling the development of higher-performance Li-ion batteries.

Author contributions

Jianghui Liu: data curation, formal analysis, investigation, writing – original draft. Shuya Liu: data curation, formal analysis. Lili Zhao: formal analysis. Yujun Luo: data curation. Yini Ran: data curation. Mohan Tang: data curation. Guilin Shi: data curation. Yuxin Liu: data curation. Jianglan Lin: data curation. Maoxian Wang: data curation. Zhengnan Li: data curation. ZhenYao: data curation. Zhusheng Yang: data curation. Hai Fu: project administration, resources, supervision, validation, writing – review & editing.

Conflicts of interest

There are no conflicts to declare.

Data availability

The data supporting this article have been included as part of the supplementary information (SI). Supplementary information is available. See DOI: https://doi.org/10.1039/d5ra10075e.

Acknowledgements

This work was supported by the National Natural Science Foundation of China (Grant No. 22561009) and Guizhou Provincial Major Science and Technology Special Project (Grant No. [2024]021), and the Lightweight Materials Engineering Research Center of the Education Department of Guizhou (Grant No. [2022]045).

References

1 F. Wu, J. Maier and Y. Yu, *Chem. Soc. Rev.*, 2020, **49**, 1569–1614.
2 M. Weiss, R. Ruess, J. Kasnatscheew, Y. Levartovsky, N. R. Levy, P. Minnmann, L. Stolz, T. Waldmann, M. Wohlfahrt-Mehrens, D. Aurbach, M. Winter, Y. Ein-Eli and J. Janek, *Adv. Energy Mater.*, 2021, **11**, 2101126.
3 Q. Li, D. Yang, H. Chen, X. Lv, Y. Jiang, Y. Feng, X. Rui and Y. Yu, *SusMat*, 2021, **1**, 359–392.

4 Y. Yao, Z. Xue, C. Li, J. Li, J. He, X. Zhang and Y. Xiang, *Energy Storage Mater.*, 2024, **71**, 103666.
5 H. Yu, X. He and X. Liang, *ACS Appl. Mater. Interfaces*, 2022, **14**, 3991–4003.
6 D.-Y. Han, I. K. Han, H. Y. Jang, S. Kim, J. Y. Kwon, J. Park, S. Back, S. Park and J. Ryu, *Energy Storage Mater.*, 2024, **65**, 103176.
7 C. Pan, S.-J. Chen, Y.-H. Huang, L. Wang, J.-L. Luo and X.-Z. Fu, *J. Power Sources*, 2022, **528**, 231207.
8 P. Zhu, D. Gastol, J. Marshall, R. Sommerville, V. Goodship and E. Kendrick, *J. Power Sources*, 2020, **485**, 229321.
9 Y. Ye, L.-Y. Chou, Y. Liu, H. Wang, H. K. Lee, W. Huang, J. Wan, K. Liu, G. Zhou, Y. Yang, A. Yang, X. Xiao, X. Gao, D. T. Boyle, H. Chen, W. Zhang, S. C. Kim and Y. Cui, *Nat. Energy*, 2020, **5**, 786–793.
10 Z. Ouyang, Y. Wang, S. Wang, S. Geng, X. Zhao, X. Zhang, Q. Xu, B. Yuan, S. Tang, J. Li, F. Wang, G. Yao and H. Sun, *Adv. Mater.*, 2024, **36**, 2401114.
11 C. Sun, R. Li, S. Weng, C. Zhu, L. Chen, S. Jiang, L. Li, X. Xiao, C. Liu, L. Chen, T. Deng, X. Wang and X. Fan, *Angew. Chem., Int. Ed.*, 2024, **63**, e202400761.
12 Y. Du, Y. Luo, K. Shi, P. Zuo, Q. Zhang, Z. Zheng, B. Sun and J. Xie, *Adv. Mater.*, 2025, **37**, 2502095.
13 Z. Ouyang, S. Wang, Y. Wang, S. Muqaddas, S. Geng, Z. Yao, X. Zhang, B. Yuan, X. Zhao, Q. Xu, S. Tang, Q. Zhang, J. Li and H. Sun, *Adv. Mater.*, 2024, **36**, 2407648.
14 Y.-E. Miao, G.-N. Zhu, H. Hou, Y.-Y. Xia and T. Liu, *J. Power Sources*, 2013, **226**, 82–86.
15 Z. Jianguo and D. Gang, *J. Thermoplast. Compos. Mater.*, 2014, **28**, 1250–1259.
16 Z.-M. Huang, Y. Z. Zhang, M. Kotaki and S. Ramakrishna, *Compos. Sci. Technol.*, 2003, **63**, 2223–2253.
17 T. Kato, Y. Yamada, Y. Nishikawa, H. Ishikawa and S. Sato, *Carbon*, 2021, **178**, 58–80.
18 C. Luo, X. Wang, J. Wang and K. Pan, *Compos. Sci. Technol.*, 2016, **133**, 97–103.
19 S. Jiang, Z. Zhou, J. Zhang, N. Yi, J. Wang, J. Zhao, L. Fan, Y. Wu and F. Gan, *Eur. Polym. J.*, 2024, **205**, 112723.
20 Y. Du, Y. Zhang, H. Xue, P. Zuo, Y. Luo and J. Xie, *Carbon*, 2024, **230**, 119622.
21 F. Wang, Y. Liu, P. Du, Z. Wang, G. Tang, P. Qin and P. Li, *J. Membr. Sci.*, 2023, **687**, 122033.
22 C. Zhang, B. Cao and P. Li, *J. Membr. Sci.*, 2018, **546**, 90–99.
23 P. Zhao, L. Cao, C. Wang, L. Zheng, Y. Li, C. Cao and Q. Huang, *Chemosphere*, 2022, 307.
24 S. Jiang, H. Hou, S. Agarwal and A. Greiner, *ACS Sustainable Chem. Eng.*, 2016, **4**, 4797–4804.
25 F. Topuz, M. A. Abdulhamid, T. Holtzl and G. Szekely, *Mater. Des.*, 2021, **198**, 109280.
26 S. Haider and I.-K. Kang, *Arab. J. Chem.*, 2018, **11**, 1165–1188.
27 X. Zhao, M. Wang, L. Xu, X. Li, F. Mo, C. Tian and L. Zhou, *RSC Adv.*, 2025, **15**, 15771–15778.
28 M. Jiang, D. Lin, W. Jia, J. Du, E. Han, M. Zhang, H. Niu and D. Wu, *Polym. Eng. Sci.*, 2021, **61**, 2691–2700.
29 V. D. Mena, X. X. F. Sánchez-Romate, M. S. Martínez and A. U. Fernández, *J. Manuf. Process.*, 2025, **155**, 323–336.
30 G.-H. Kang, M. Kim and Y.-B. Park, *Polym. Test.*, 2023, **126**, 108138.
31 Q. Zhang, Y. Xu, Y. Yang, L. Li, C. Song and X. Su, *J. Polym. Eng.*, 2018, **38**, 147–156.
32 J.-W. Zha, F. Sun, S.-J. Wang, D. Wang, X. Lin, G. Chen and Z.-M. Dang, *J. Appl. Phys.*, 2014, **116**, 134104.
33 X. Yu, S. Ma, Q. Zhang, Y. Hou, Q. He, Y. Luo and X. Gao, *Eur. Polym. J.*, 2023, **190**, 111989.
34 N. Li, J. Zhao, Y. Zhang, R. Song, N. Zhang, Y. Cui, J. Lin, H. Xu and Y. Huang, *Adv. Funct. Mater.*, 2024, **35**, 2419102.
35 B. Zaidi, N. Smida, M. G. Althobaiti, A. G. Aldajani and S. D. Almdhaibri, *Polymers*, 2022, **14**, 1093.
36 Y. Mei, J. Zhou, Y. Hao, X. Hu, J. Lin, Y. Huang, L. Li, C. Feng, F. Wu and R. Chen, *Adv. Funct. Mater.*, 2021, **31**, 2106676.
37 Y. Ouyang, X. Li, F. Ding, L. Bai and F. Yuan, *Compos. Sci. Technol.*, 2020, **190**, 108019.
38 D. Wei, W. Shen, T. Xu, K. Li, L. Yang, Y. Zhou, M. Zhong, F. Yang, X. Xu, Y. Wang, M. Zheng, Y. Zhang, Q. Li, Z. Yong, H. Li and Q. Wang, *Mater. Today Energy*, 2021, **23**, 100889.
39 J. C.-M. Chen, J. Yang and M. M.-C. Cheng, *J. Power Sources*, 2019, **430**, 169–174.
40 M. Shimizu, T. Ohnuki, T. Ogasawara, T. Banno and S. Arai, *RSC Adv.*, 2019, **9**, 21939–21945.
41 J. Wang, Z. Shen and M. Yi, *Carbon*, 2019, **153**, 156–163.
42 X. Wei, Y. Guan, X. Zheng, Q. Zhu, J. Shen, N. Qiao, S. Zhou and B. Xu, *Appl. Surf. Sci.*, 2018, **440**, 748–754.
43 X. Li, L. Wang, C. Li, B. Chen, Q. Zhao and G. Zhang, *J. Power Sources*, 2016, **308**, 65–74.
44 G.-H. An, S. Cha and H.-J. Ahn, *Appl. Surf. Sci.*, 2019, **478**, 435–440.
45 D.-Y. Shin, D.-H. Park and H.-J. Ahn, *Appl. Surf. Sci.*, 2019, **475**, 519–523.
46 K. Wang, S. Luo, Y. Wu, X. He, F. Zhao, J. Wang, K. Jiang and S. Fan, *Adv. Funct. Mater.*, 2012, **23**, 846–853.
47 N. El Halya, Y. Seffar, M. Aqil, J. Alami and M. Dahbi, *RSC Adv.*, 2025, **15**, 37371–37378.
48 P. Xiao, Z. Wang, K. Long, J. Yang, X. Liu, C. Ling, L. Chen and L. Mei, *RSC Adv.*, 2024, **14**, 13277–13285.
49 S. Kim and G. H. An, *Int. J. Energy Res.*, 2022, **46**, 16658–16669.
50 C. Li, K. Cai, L. Liang, J. Dong, X. Liu, N. Cao, Q. Shao and X. Zang, *Energy Technol.*, 2022, **10**, 2200150.